Hierarchical non-negative matrix factorization to characterize brain tumor heterogeneity using multi-parametric MRI

Nicolas Sauwen[1,2], Diana M Sima[1,2], Sofie Van Cauter[3], Jelle Veraart[4,5], Alexander Leemans[6], Frederik Maes[2,7], Uwe Himmelreich[8], Sabine Van Huffel[1,2]

[1] KU Leuven, Department of Electrical Engineering (ESAT), STADIUS Centre for Dynamical Systems, Signal Processing and Data Analytics, Leuven, Belgium
[2] iMinds Medical IT, Leuven, Belgium
[3] Department of Radiology, University Hospitals of Leuven, Leuven, Belgium
[4] iMinds Vision Lab, Department of Physics, University of Antwerp, Antwerp, Belgium
[5] Center for Biomedical Imaging, Department of Radiology, New York University Langone Medical Center, New York, NY, USA
[6] Image Sciences Institute, University Medical Center Utrecht, Utrecht University, Utrecht, Netherlands
[7] KU Leuven, Department of Electrical Engineering (ESAT), PSI Centre for Processing Speech and Images, Leuven, Belgium
[8] Biomedical MRI/MoSAIC, Department of Imaging and Pathology, KU Leuven, Leuven, Belgium

Word count: *10053*

Keywords: *Multimodality imaging, Dynamic contrast methods, High order diffusion MR methods, Spectroscopic imaging, Head and neck cancer, Non-negative matrix factorization*

List of abbreviations: *ADC: apparent diffusion coefficient; aHALS: accelerated hierarchical alternating least squares; Cho: total choline; cMRI: conventional magnetic resonance imaging; Cre: total creatine; CSF: cerebro-spinal fluid; DKI: diffusion kurtosis imaging; DSC-MRI: dynamic susceptibility-weighted contrast-enhanced magnetic resonance imaging; DTI: diffusion tensor imaging; DWI: diffusion-weighted imaging; FA: fractional anisotropy; FLAIR: fluid-attenuated inversion recovery; FOV: field of view; FWHM: full width at half maximum; GBM: glioblastoma multiforme; Glx: glutamine+glutamate; Gly: glycine; HGG: high-grade glioma; ^{1}H-MRSI: proton magnetic resonance spectroscopic imaging; hNMF: hierarchical non-negative matrix factorization; Lac: lactate; LGG: low-grade glioma; Lip: lipids; MD: mean diffusivity; mI: myo-inositol; MK: mean kurtosis; MP-MRI: multi-parametric magnetic resonance imaging; NAA: N-acetyl-aspartate; NMF: non-negative matrix factorization; PWI: perfusion-weighted imaging; rCBV: relative cerebral blood volume; ROI: region of interest; T1+C: contrast-enhanced T1; VOI: volume of interest; WHO: World Health Organization*

Abstract

Tissue characterization in brain tumors and in particular in high-grade gliomas is challenging due to the co-existence of several intra-tumoral tissue types within the same region and the high spatial heterogeneity. This study presents a method for the detection of the relevant tumor substructures (i.e. viable tumor, necrosis and edema), which could be of added value for the diagnosis, treatment planning and follow-up of individual patients. Twenty-four glioma patients (10 low-grade gliomas (LGG), 14 high-grade gliomas (HGG)) underwent a multi-parametric MRI (MP-MRI) scheme, including conventional MRI (cMRI), perfusion-weighted imaging (PWI), diffusion kurtosis imaging (DKI) and short-TE ^{1}H-MRSI. MP-MRI parameters were derived: T2, T1+contrast, FLAIR, relative cerebral blood volume (rCBV), mean diffusivity

(MD), fractional anisotropy (FA), mean kurtosis (MK), and the principal metabolites: lipids (Lip), lactate (Lac), N-acetyl-aspartate (NAA), total choline (Cho), etc. Hierarchical non-negative matrix factorization (hNMF) is applied to the MP-MRI parameters, providing tissue characterization on a patient-by-patient and voxel-by-voxel basis. Tissue-specific patterns are obtained and the spatial distribution of each tissue type is visualized by means of abundance maps. Dice-scores were calculated by comparing tissue segmentation derived from hNMF to the manual segmentation by a radiologist. Correlation coefficients were calculated between each pathologic tissue source and the average feature vector within the corresponding tissue region. For the HGG patients, mean Dice-scores of 78%, 85% and 83% were obtained for viable tumor, the tumor core and the complete tumor region. The mean correlation coefficients were 0.91 for tumor, 0.97 for necrosis and 0.96 for edema. For the LGG patients, mean Dice-score of 85% and mean correlation coefficient of 0.95 were found for the tumor region. hNMF was also applied to reduced MRI datasets, showing the added value of individual MRI modalities.

Introduction

Neuro-imaging has become an indispensable tool when it comes to the diagnosis, treatment planning and follow-up of brain tumor patients. Conventional magnetic resonance imaging (cMRI) is the imaging modality of choice upon suspicion of a brain tumor. cMRI allows for localization of the lesion and assessment of radiological features like contrast enhancement and presence of necrosis, which might aid in establishing differential diagnosis. However, in a significant number of cases, cMRI is unable to provide reliable diagnosis and grading (1), which is crucial for optimal treatment planning and prognosis.

The international classification system published by the World Health Organization (WHO) based on histopathology is currently recognized as the gold standard for classifying brain tumors (2). Tumor grading is based on histological criteria such as cell density, nuclear atypia, mitosis, necrosis and endothelial proliferation. High-grade gliomas are known to show intra-tumoral heterogeneity, with spatial differences in cellular phenotype and malignancy grade (3,4). Due to this heterogeneity, there is a risk of underdiagnosing as biopsy sampling might not represent the most malignant part of the tumor (5). Intra-tumoral heterogeneity is not adequately reflected in cMRI (4), making it an improper tool for biopsy targeting. It is estimated that up to 25% of brain tumors are undergraded because the most malignant part of the tumor may not enhance after contrast administration (6).

Over the past decade, advanced MRI modalities, such as perfusion-weighted imaging (PWI), diffusion-weighted imaging (DWI) and MR spectroscopic imaging (MRSI) have gained interest in the clinical field, and their added value regarding brain tumor diagnosis, treatment planning and follow-up has been recognized (7).

PWI assesses the hemodynamics of brain tumors. More specifically, it proposes to measure the degree of tumor angiogenesis, and possibly capillary permeability, as the blood-brain barrier is disrupted in the newly-formed glioma microvessels. HGGs are known to promote vascular ingrowth, resulting in increased microvascular density and blood volume. Moreover, the newly-formed vessels within a tumor are more coarse and tortuous compared to normal vessels, and they show increased vascular permeability (8). Relative cerebral blood volume (rCBV) is considered the most relevant parameter for studying brain tumors (9). In astrocytomas, a strong correlation between rCBV and tumor grade has been reported (8,10), with rCBV values increasing along with the tumor grade. Nevertheless, there exists substantial intragrade

variability of rCBV that increases with tumor grade. In addition, oligodendrogliomas may present with high rCBV regardless of grade (11). The endothelial transfer coefficient K^{trans}, derived from pharmacokinetic modelling applied to T1-weighted dynamic contrast-enhanced MRI, is considered an indicator of vascular permeability. K^{trans} has been related to glioma grade (12), suggesting increased blood-brain barrier disruption with increasing tumor grade. rCBV measurements in the peri-tumoral region have been shown to differentiate glioblastoma multiforme (GBM) from metastases, suggesting the detection of tumor infiltration (10,13). Furthermore, several studies have suggested that maximum tumoral rCBV might be an indicator of the most malignant part of the tumor for biopsy targeting (14,15).

Proton MRSI (^{1}H-MRSI) provides biochemical information regarding the spatial distribution of metabolites in a localized region of the brain. The principal metabolites found in brain tumors include lipids (Lip), lactate (Lac), N-acetyl-aspartate (NAA), glutamine+glutamate (Glx), total creatine (Cre), total choline (Cho), glycine (Gly) and myo-inositol (mI). Statistically significantly higher metabolite ratios of Cho/Cre and Cho/NAA have been reported in HGGs compared to LGGs (16). Lipids are a hallmark of necrosis, hence elevated Lip levels are seen almost exclusively in HGGs, particularly in GBMs (17). Nevertheless, considerable overlap between LGG and HGG metabolite levels has been demonstrated. Sites with elevated levels of Cho or Cho/NAA have been proposed as biopsy targets and have been reported to increase the accuracy of tumor biopsy (18,19). MRSI measurements in peri-tumoral edema surrounding GBMs have shown increased Cho levels, suggesting tumor infiltration (13,20).

DWI aims at visualizing the mobility of water molecules within tissue due to Brownian motion. The apparent diffusion coefficient (ADC) relates to the mean path length of water diffusion within each tissue voxel (21). Several reports have shown that minimum ADC values correlate inversely with glioma grade, probably because of increasing tumor cellularity with increasing grade (22,23). Nevertheless, substantial overlap in ADC values among different grades limit its clinical applicability. Diffusion tensor imaging (DTI) is used to describe diffusion anisotropy. Two DTI metrics characterize the three-dimensional variability of the diffusion process: mean diffusivity (MD) and fractional anisotropy (FA) (24). Significant differences in MD and FA have been reported among pathologic tissue types in HGGs (25). Diffusion kurtosis imaging (DKI) is an extension of DTI, taking into account the non-Gaussian component of the diffusion process due to diffusion restriction. In isotropic tissue, this non-Gaussian diffusivity can be quantified by the mean kurtosis (MK) value (26). Furthermore, it has been demonstrated that DKI provided more accurate estimates of MD and FA than DTI (27). First results of using DKI for grading and differential diagnosis of brain tumors look promising (28,29).

The recent emergence of advanced MRI techniques has allowed us to learn much more about brain tumors in a non-invasive way. Many studies have investigated the potential of individual MRI modalities to characterize tumor grade, detect full tumor extent and assess early success of therapy. Although the added value of PWI, DWI and MRSI is unmistakable, it has become clear that no modality in itself is specific enough to answer these clinical questions unambiguously. This conclusion has led towards multi-parametric MRI (MP-MRI), i.e. the combination of several MRI modalities to provide complementary information on the structural, hemodynamic and/or biochemical characteristics of the tissue. Several studies have shown that MP-MRI improves diagnostic accuracy when it comes to grading gliomas compared to individual MRI modalities (7,15,30). Other studies have reported improved differentiation of intra-tumoral and peri-tumoral tissue types by applying supervised classification methods to MP-MRI data (31,32). Although the spatial heterogeneity of HGGs is partially explained by the presence of different stages of the disease throughout the lesion (3), it is also attributed to

the co-existence of several intra-tumoral tissue types within the same region, such as the presence of focal necrosis within viable tumor tissue (33), tumor infiltration in peri-tumoral edema (13) and the formation of vasogenic edema in the viable tumor region (34). Therefore, characterization of the tumoral and peri-tumoral tissue might benefit from a model that incorporates the concept of tissue mixtures. Blind source separation techniques have been applied to brain tumor MRSI data for this purpose. In particular, non-negative matrix factorization (NMF) methods have been shown to give most promising results (35,36). NMF aims to extract physically meaningful sources, corresponding to tissue-specific patterns. NMF assesses the relative contribution of each tissue type within each voxel, assuming the dataset can be modelled as a linear combination of the constituent tissue types. In this study, a hierarchical NMF technique is presented and applied to an MP-MRI dataset combining cMRI, PWI, ^{1}H-MRSI and DKI to characterize tumor heterogeneity, providing a comprehensive representation of the spatial distribution of tissue types in the tumor region. Limited user interaction is required for specifying the number of tissue types present in the region of interest. Although voxels of mixed tissue contributions are allowed, the method benefits from the assumption that a large number of voxels will contain mainly one tissue type, given the relatively high resolution of cMRI, at which all MRI maps are resampled. Tissue-specific patterns are obtained on a patient-by-patient basis. The usage of MP-MRI data provides a detailed tissue characterization and delimitation at the cMRI voxel level, and is able to improve source separation of the different tissue types. To assess the added value of individual MRI modalities, hNMF is also applied to reduced MP-MRI datasets, leaving out one modality at a time, and to cMRI data only.

Methodology

Patient population

The institutional human ethics review board approved this prospective study. Written informed consent was obtained from every patient before participation. We examined 24 patients with suspicion of glioma based on conventional radiological imaging, prior to any treatment (9 females/15 males; age range: 22–78 years, median age: 55 years). We enrolled 14 patients with a HGG, of whom 11 had grade IV glioma (GBM) and 2 had grade III glioma. One patient had a grade II astrocytoma with focal progression to a grade III glioma. Ten patients with a LGG were recruited. Of these 10 patients, 1 was diagnosed with a diffuse fibrillary glioma grade II, 3 with a grade II astrocytoma, 2 with a grade II oligodendroglioma, 1 with a grade II oligoastrocytoma, 1 with a grade II lesion with mixed findings of pilocytic astrocytoma, angiocentric glioma, and oligodendroglioma, and 2 with grade I oligodendroglioma. The lesions were classified according to grade using the 2007 WHO classification (2), with histopathological confirmation in all cases.

Data acquisition and analysis

MRI acquisition was performed on a 3T MR system (Philips Achieva, The Netherlands), using a body coil for transmission and an 8-channel head coil for signal reception. The total scanning time for all MRI modalities was 45min.

cMRI

An axial spin echo T2-weighted MRI was acquired with the following parameters: repetition time (TR)/ echo time (TE): 3000/80ms; slice/gap: 4/1 mm; turbo factor: 10; field of view [FOV]: 230×184mm^2; acquisition matrix: 400×300.

A T1-weighted 3D spoiled gradient echo MRI scan with contrast administration was performed with the following parameters: fast field echo, TR/TE/inversion time (TI): 9.7/4.6/900ms; flip angle: 8°; turbo field echo factor: 180; acquisition voxel size: 0.98×0.98×1mm^3; 118 contiguous partitions.

An axial FLAIR MRI scan was acquired with the following parameters: TR/TE/TI: 11000/120/2800 msec, slice/gap: 4/1 mm, FOV: 230×184mm², acquisition matrix: 240×134.

PWI

Perfusion images were obtained using Dynamic Susceptibility-weighted Contrast-enhanced (DSC) MRI with a gradient-echo EPI sequence: TR/TE: 1350/30ms; slice/gap: 3/0mm; dynamic scans: 60; FOV: 200×200mm^2; matrix: 112×109; scan time: 1min26s. EPI data were acquired during the first pass following a rapid injection of a 0.1mmol/kg body weight bolus of meglumine gadoterate (Dotarem, Guerbet, France) via a mechanical pump at a rate of 4mL/s, followed by a 20-mL bolus of saline.

DSC data were analyzed using the DSCoMAN plugin (37) in ImageJ (38). rCBV maps were derived from the dynamic signal intensity curves using the method proposed by Boxerman et al. (39). To correct for contrast agent extravasation, the relaxivity-time curve in each voxel is approximated as a linear combination of the whole-brain average curve in the non-enhancing voxels and its time integral, with the first term representing the uncontaminated relaxivity change and the second term reflecting the effect of leakage. The coefficients of this linear combination are found in each voxel using linear least-squares fitting.

MRSI

A 2D-^{1}H MRSI protocol was used as previously described (40). A point-resolved spectroscopy sequence was used as the volume selection technique with a bandwidth of 1.3kHz for the conventional slice-selective pulses; TR/TE: 2000/35ms; FOV: 160×160mm^2; maximal volume of interest (VOI): 80×80mm^2; slice thickness: 10mm; acquisition voxel size: 10×10mm^2; reconstruction voxel size: 5×5mm^2; receiver bandwidth: 2000Hz; samples: 2048; number of signal averages: 1; water suppression method: multiple optimizations insensitive suppression train (41); first- and second-order pencil beam shimming; parallel imaging: sensitivity encoding with reduction factors of 2 (left-right) and 1.8 (anterior-posterior); scan time: 3min30s. Automated pre-scanning optimized the shim in order to yield a peak width consistently under 20Hz full-width half-maximum (FWHM). The slice was positioned in the center of the tumor.

The raw MRSI data were exported from the Philips platform after standard post-processing (zero-filling in k-space, transformation from k-space to spatial domain, automatic phase correction and eddy current correction). Further processing was done with the in-house SPID software (42) in MatLab 2012b (MathWorks, Massachussets, USA). AQSES-MRSI (43) was used to quantify the following metabolites using an experimentally acquired metabolite basis set: Lip at 1.3ppm, Lac, NAA, Glx, Cre, Cho, mI and Gly. The basis set incorporates prior knowledge of the individual metabolites into the quantification procedure, i.e. their frequency, phase, and relative amplitudes within the multiplets. MPFIR (Maximum-Phase Finite Impulse Response) filtering (44) was included in the AQSES-MRSI procedure for residual water suppression: the model order was set to 25 and the spectral range from 0.25 to 4.2ppm. A band of voxels at the outer edges of the VOI was omitted to avoid chemical shift displacement artifacts and lipid contamination (band proportional to the grid size, maximally 3 voxels wide for a 16×16 grid).

DKI

An EPI DWI sequence with a spin-echo readout was used to acquire the DKI data, according to an optimized DKI protocol (26). Implemented b-values were 0, 700, 1000, and 2800s/mm^2, applied in respectively 10, 25, 40, and 75 uniformly distributed directions. The following parameters were used throughout the DKI acquisition sequence: TR/TE: 3200/90ms; gradient duration/diffusion time interval: 20/48.3ms; FOV: 240×240mm^2; matrix: 96×96; number of signal averages: 1; slice/gap: 2.5/0mm; parallel imaging: SENSE with factor 2 in the antero-posterior direction. The scan time was 17min30s.

After motion and eddy current correction (45), isotropic smoothing was applied using a Gaussian kernel (FWHM=3mm) to reduce Gibbs ringing. However, smoothing was applied to the b=0 and b=700 images only, so as not to alter the nature of the noise distribution in the highly diffusion-weighted images in order to avoid a noise bias in the subsequent tensor estimation (46). Diffusion and kurtosis tensors were estimated in each voxel using a constrained weighted linear least-squares algorithm (46). MD, FA and MK maps were derived from the tensors according to (26,47).

Data coregistration

All MRI datasets were coregistered and brought to the same spatial resolution to perform voxel-wise analysis. Cubic spline interpolation was used to create an interpolated set of T1+C images, with one slice coinciding with the central plane of the MRSI VOI. Only the MRI data of this central slice within the MRSI region of interest (ROI) were considered for hNMF analysis, as no MRSI data were available outside of this ROI. Skull-stripping was applied to all images prior to coregistration. The cMRI datasets and the PWI dataset were rigidly coregistered to the interpolated T1+C reference set using SPM (48). The normalized mutual information criterion was used for coregistration (49), with cubic spline interpolation for reslicing. A nonlinear coregistration of the diffusion-weighted parameter maps to the coregistered T2-weighted MRI dataset was performed using ExploreDTI (50) to minimize the local misalignment between the EPI distorted DKI data and the cMRI data. The quantified metabolite values were allocated to the centre of the corresponding voxels of the original MRSI grid prior to interpolation. The MRSI data were spatially aligned with the reference set and resampled using cubic spline interpolation.All MRI parameters were brought to the spatial resolution of the original T1+C dataset, i.e. 0.98×0.98×1mm^3.

Hierarchical Non-Negative Matrix Factorization

NMF is a blind source separation technique (51), in which a matrix X is approximately factorized into the product of a source matrix W and an abundance matrix H:

$$X_{n\times m} \approx W_{n\times r} \times H_{r\times m} \quad [1]$$

X contains a set of non-negative data, with m data points on its columns and n features per data point on its rows. The columns of W represent the r sources. Each row of H contains the abundance values of the corresponding column in W. In this way, NMF describes each voxel's feature vector by a linear combination of a predefined number of sources. Characterization of the tumor heterogeneity based on MP-MRI can be seen as an NMF-problem as follows: for each voxel within the MRSI ROI (as only these voxels have a full MP-MRI dataset), the corresponding MRI features are stacked in a vector. The obtained vectors are then grouped as columns of a matrix X, such that each column of X represents a set of MRI features for one

particular voxel. Such a feature set can then be approximated as a linear mixture of a certain number of tissue types, each of which is characterized by a tissue-specific pattern. NMF is an unsupervised learning method, meaning that it can be applied on a patient-by-patient basis.

The mathematical formulation of the basic NMF problem to perform the factorization in Equation[1] is given by:

$$\min_{W,H} f(W,H) = \frac{1}{2}\left\|X - WH\right\|_F^2 \quad [2]$$

such that: $\forall i, j:\ W_{i,j}, H_{i,j} \geq 0$

where $\left\| \ \right\|_F$ represents the Frobenius norm. In our study the accelerated hierarchical alternating least squares (aHALS) NMF implementation was used (52). aHALS was proven superior to other NMF implementations in a study to characterize brain tumors using simulated MRSI data (53).

The MRI parameters discussed in the previous section were used as input features: T2, T1+C, FLAIR, rCBV, Lip, Lac, NAA, Glx, Cre, Cho, mI, Gly, MD, FA and MK. To all non-metabolic MRI maps, smoothing was applied using moving average windows with kernel sizes of 3×3 and 5×5. These smoothed MRI maps were also added to the feature set, resulting in a total of 29 features (8 metabolic features, 7 non-metabolic features and 14 smoothed non-metabolic features). The metabolic features were rescaled by dividing them by the maximum metabolite value throughout the MRSI ROI, such that relative amplitudes were unchanged between the different metabolites. For the non-metabolic features, each feature's full range was rescaled to [0 1].

The hNMF procedure consists of three steps. Fig.1 gives a schematic overview of the hNMF procedure and the individual steps are discussed in detail below.

Step1

A rank-2 NMF analysis is performed on all voxels in the MRSI ROI. This results into 2 sources, source1^{step1} and source2^{step1}, and their corresponding abundance maps (H-maps). It is assumed that the pathologic tissue types (viable tumor and possibly necrosis or edema) and the normal tissue types (white matter, gray matter, cerebro-spinal fluid (CSF), blood vessels,...) present in the ROI will be divided over these 2 sources. Consequently, voxels with a dominant tissue type will have a higher abundance for the source that represents their tissue type. As NMF suffers from scaling ambiguities, each H-map was rescaled such that the maximum abundance value over all voxels was set to 1 for each source. The sources were rescaled accordingly. Rescaling of the H-maps makes the voxel assignment in step2 reproducible and robust against possible scaling imbalances between source1 ^{step1} and source2 ^{step1}.

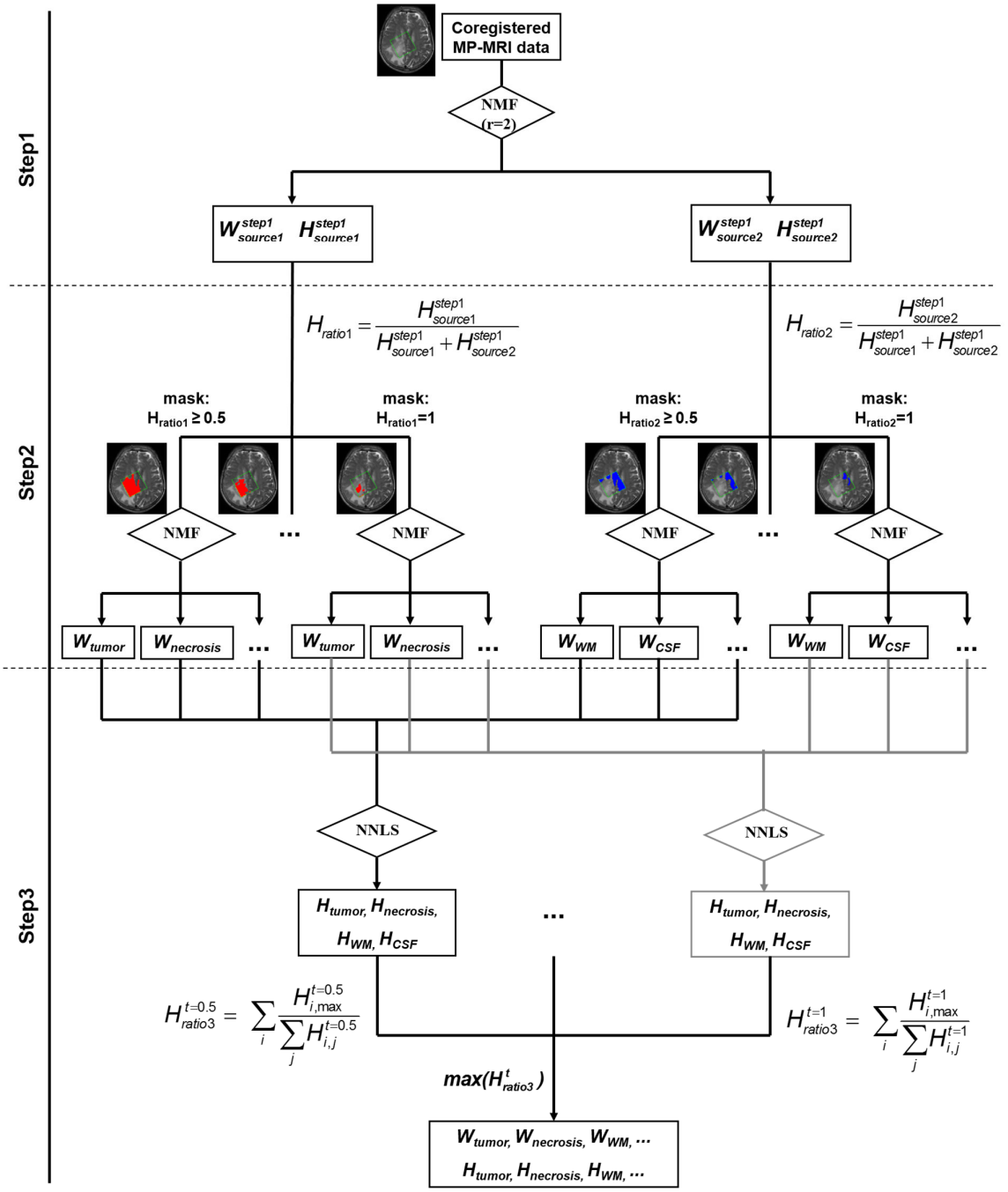


Figure 1: Schematic overview of the hNMF procedure.
[NNLS: Non-negative least-squares]

Step2

Tissue-specific patterns are found by applying a second level of NMF to the regions represented by source1^{step1} and source2^{step1}. Based on visual inspection of the cMRI data by an experienced neuro-radiologist, the number of tissue types present in the ROI was determined. Each tissue type was then assigned to either source1^{step1} or source2^{step1} by considering which source showed the highest abundance values in the corresponding tissue region. An iterative voxel selection is

considered for both tissue regions, based on voxel-wise abundance ratio maps calculated over the whole ROI:

$$H_{i,ratio1} = \frac{H_{i,source1^{step1}}}{H_{i,source1^{step1}} + H_{i,source2^{step1}}} \quad [3] \qquad \text{and} \qquad H_{i,ratio2} = \frac{H_{i,source2^{step1}}}{H_{i,source1^{step1}} + H_{i,source2^{step1}}} \quad [4]$$

with $H_{i,source1^{step1}}$ the abundance of source1^{step1} at voxel i and $H_{i,source2^{step1}}$ the abundance of source2^{step1} at voxel i. We then consider a variable threshold t to define a mask on the H_{ratio1} and H_{ratio2} map. At each fixed value of t, NMF is applied to the group of voxels with H_{ratio1} larger than t for source1^{step1} and to the group of voxels with H_{ratio2} larger than t for source2^{step1}. We let t range from 0.5 to 1, with t=0.5 corresponding to voxels with equal abundances for source1^{step1} and source2^{step1} and t=1 corresponding to voxels with a nonzero abundance for only one of the sources. As t increases, only voxels that have a more clear dominant source are withheld for the second level of NMF. In this way, tissue types represented by source1^{step1} do not have to fit voxels that contain significant contributions of tissue types represented by source2^{step1} and vice-versa, minimizing cross-contamination between the tissue sources. The t-interval was divided into 20 steps, as a finer step size did not significantly improve the results any further. From this range of t-values, the optimal t is determined based on a sparsity criterion in hNMF step3.

Step3

For each value of t, the tissue-specific patterns obtained from both regions are then re-combined to calculate the abundances over the whole ROI using non-negative least-squares fitting. To automatically determine the optimal threshold value t, a criterion that promotes sparsity to the voxel-wise tissue abundances is introduced. The optimal threshold t then corresponds to the highest H^t_{ratio3} value, where:

$$H^t_{ratio3} = \sum_i \frac{H^t_{i,\max}}{\sum_j H^t_{i,j}} \quad [5]$$

with $H^t_{i,j}$ denoting the abundance of source j in voxel i after the second level of NMF at threshold t and $H^t_{i,\max}$ denoting the highest abundance in voxel i at threshold t. In [5], the summation over i covers the whole ROI and the sum in the denominator goes over all the sources j. A higher value of H^t_{ratio3} can be interpreted as a more sparse solution: on average, the voxels will have a more dominant tissue type. The final hNMF factorization is the one belonging to the optimal threshold t. For each NMF analysis, the W- and H-matrix were initialized randomly. As NMF is a non-convex optimization problem, the full hNMF procedure was repeated 20 times for each patient, and the output with the highest H_{ratio3} was withheld.

To verify the robustness of the hNMF algorithm when less MRI modalities are available, hNMF was not only applied to the full MP-MRI dataset but also to 5 reduced MRI datasets: 4 reduced MP-MRI datasets by omitting consecutively the cMRI, PWI, MRSI and DKI data from the full MP-MRI dataset, and one dataset considering only the cMRI data.

Validation

Dice score

For each patient, a tissue segmentation was obtained from the abundance maps, assigning each voxel to 1 tissue class. This was done by applying k-means clustering to the *H*-values, with *k* set to the number of tissue types resulting from hNMF. Each cluster was initialized with one *H*-value set to 1 and all others set to 0. The segmentation obtained from hNMF was compared to the manual segmentation by a radiologist (SVC, with 6 years of experience in brain tumor research) using the Dice score:

$$Dice_{tissue} = 2 \times \frac{A_{tissue,hNMF} \cap A_{tissue,radiol}}{A_{tissue,hNMF} + A_{tissue,radiol}} \quad [6]$$

with $A_{tissue,hNMF}$ the area of the tissue region as defined by hNMF and $A_{tissue,radiol}$ the area as defined by the radiologist. For comparability of the results, Dice-scores are reported for pathologic tissue classes similar to those in the BRATS challenge (54): tumor (viable tumor), tumor core (viable tumor + necrosis) and complete tumor (viable tumor + necrosis + edema).

Correlation coefficient

The validation of the sources is based on the hypothesis that the sources correspond to actual tissue types. The average feature vector was calculated over all voxels belonging to the same tissue type, based on the radiologist's segmentation. Correlation coefficients were calculated as the inner product between the normalized average feature vector and the corresponding normalized source obtained from hNMF. Correlation values were calculated for tumor, necrosis and edema.

Statistical analysis

The mean, standard deviation and range of the Dice-scores and correlation coefficients are reported for the HGG and LGG group of patients. To assess whether improved tissue differentiation was statistically significant for all MR modalities compared to the reduced MRI datasets, the non-parametric one-tailed Wilcoxon signed rank test was applied. A statistical significance level of $p<0.05$ was considered.

Results

An illustration of the hNMF analysis is given below for a representative GBM patient. Fig.2 shows some of the relevant MRI features as well as the hNMF results for the full MP-MRI dataset for patient 16. hNMF results are only shown for the 3 pathologic tissue types: tumor, necrosis and edema. Fig.3 compares the abundance maps of tumor and necrosis for patient 16 for the full and the 5 reduced MRI datasets, as well as the resulting segmentations for viable tumor and the tumor core. Best segmentation results were obtained with the full MP-MRI dataset and the no-PWI dataset, both giving similar abundance maps and hNMF segmentations. For the no-cMRI case, tumor segmentation was reduced, missing a larger portion of the manual delineation. For no-MRSI, some voxels outside the pathologic region were assigned to the tumor core. In the case of no-DKI, a small portion of edema adjacent to the tumor region was labelled as tumor. Performance was clearly lowest when considering cMRI only, where necrosis could no longer be differentiated from edema and voxels outside the pathologic region were assigned to the tumor core. The detailed hNMF results of all patients for the full MP-MRI dataset, as well as the individual Dice-scores and correlation coefficients for all considered MRI datasets can be found in Appendices A and B.

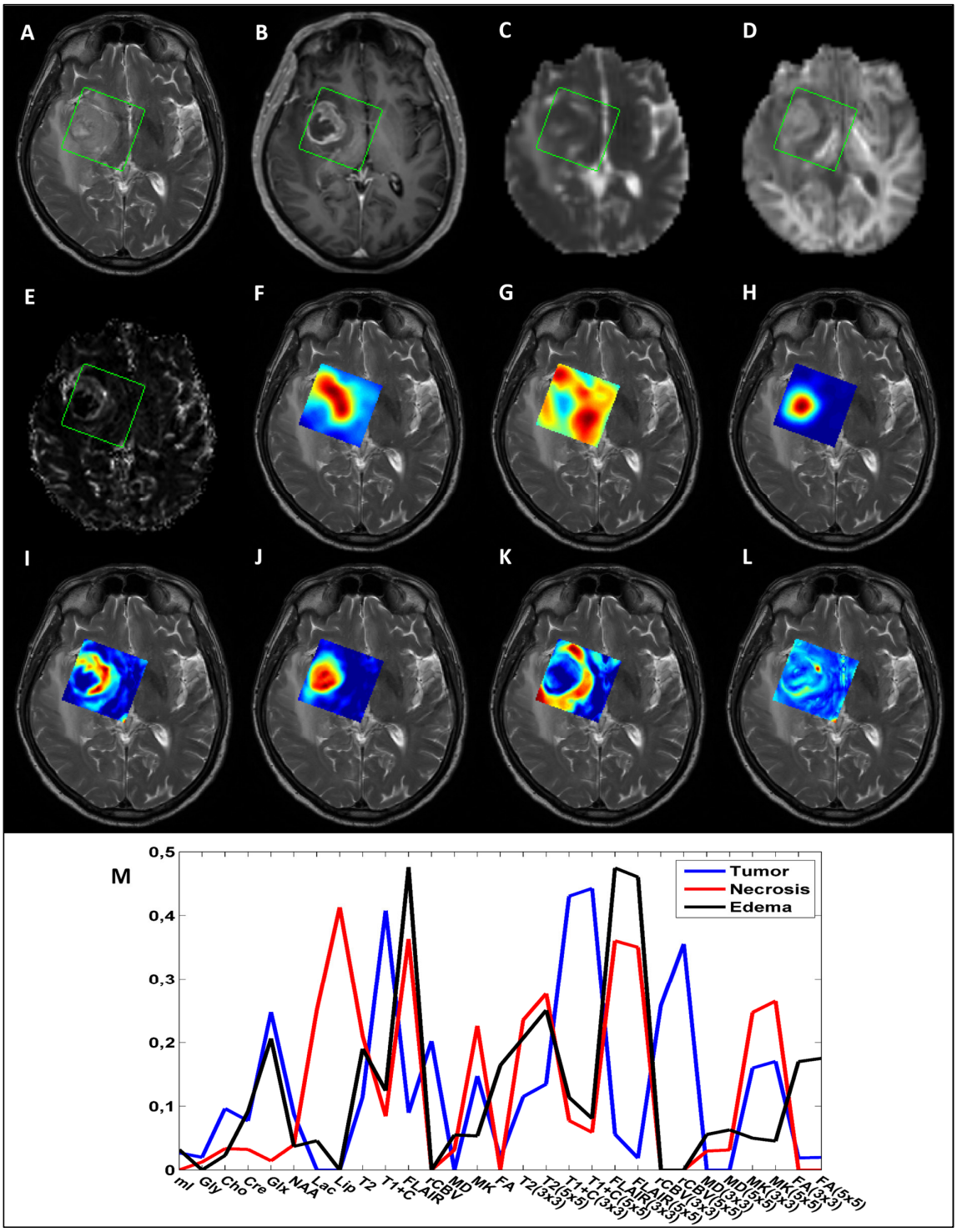


Figure 2: Coregistered MRI maps of different modalities and hNMF results for GBM patient 16. The shown input maps are T2 (A), T1+C (B), MD (C), MK (D), rCBV (E), Cho (F), Cre (G) and Lip maps (H). The green box indicates the MRSI ROI. hNMF abundance maps are shown for tumor (I), necrosis (J) and edema (K). The error map is shown in (L) and the pathologic hNMF sources in (M).

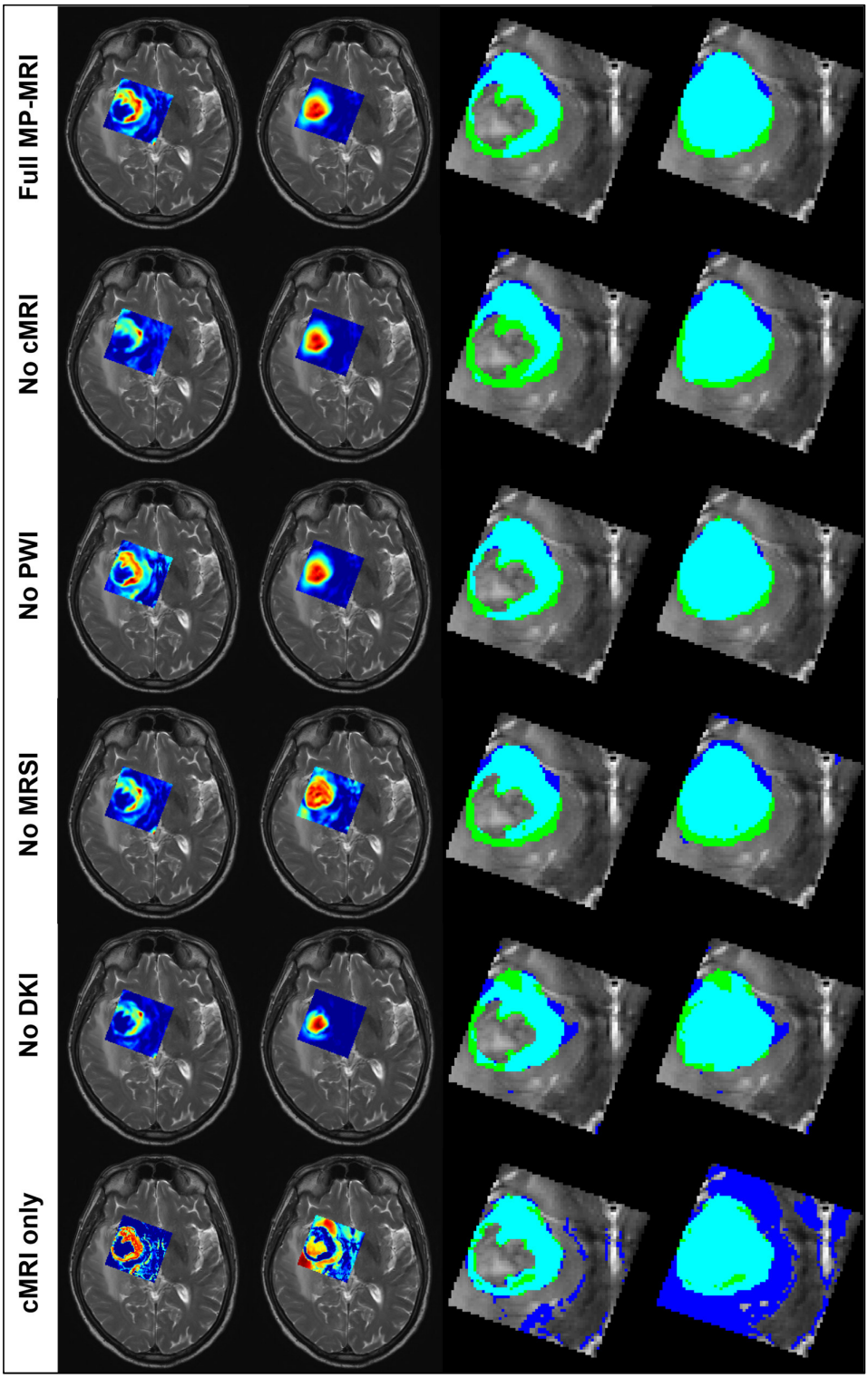


Figure 3: Comparison of the hNMF results for the different MRI datasets for GBM patient 16. hNMF abundance maps are shown for tumor and necrosis. Comparisn of the segmentation by the radiologist (blue) and obtained with hNMF (green) is shown for all MRI datasets for tumor and for the tumor core. Cyan indicates segmentation overlap.

Table 1 reports the mean, standard deviation and range of the Dice-scores for tumor, the tumor core and the complete tumor region of the HGG patients for all considered datasets. For the full MP-MRI dataset, mean Dice-scores of 78%, 85% and 83% were found for tumor, tumor core and complete tumor, respectively. Lower mean Dice-scores were found for all reduced MRI datasets for the 3 tissue classes. Nevertheless, statistical significance could not be shown in a few cases: for the no-PWI case for tumor and tumor core, and for the no-DKI case for tumor. Considering the 4 reduced MP-MRI datasets, the lowest mean Dice-scores are found for no-cMRI. Especially for tumor, a decrease of 13% was found compared to full MP-MRI. Besides that, the decrease in mean Dice-score ranged between 2% and 8% for the 3 tissue classes for the reduced MP-MRI datasets. When considering only cMRI, a larger decrease of the Dice-scores is found: 9% for tumor, 14% for tumor core and 15% for complete tumor. The standard deviation is lower and the minimum Dice-score is higher for full MP-MRI for each tissue class compared to the reduced datasets.

Table1: *Mean, standard deviation and range of the Dice-scores for the HGG patients. Results are reported for tumor, the tumor core and the complete tumor region using the full MP-MRI dataset (light grey), MP-MRI without cMRI, PWI, MRSI and DKI and for cMRI data only. P-values report statistical significance of higher Dice-scores for the full MP-MRI dataset (* indicates statistical significance for p<0.05).*

	Dice-score tumor [%]						**Dice-score tumor core [%]**						**Dice-score complete tumor [%]**					
	All	**no-cMRI**	**no-PWI**	**no-MRSI**	**no-DKI**	**cMRI only**	**All**	**no-cMRI**	**no-PWI**	**no-MRSI**	**no-DKI**	**cMRI only**	**All**	**no-cMRI**	**no-PWI**	**no-MRSI**	**no-DKI**	**cMRI only**
Mean	**78**	**65**	**76**	**71**	**76**	**69**	**85**	**77**	**81**	**79**	**79**	**71**	**83**	**75**	**79**	**76**	**77**	**68**
Standard deviation	10	14	19	16	12	18	11	14	18	17	14	17	14	15	17	18	14	18
Range [Min-Max]	59-93	39-91	20-93	43-93	56-92	38-91	54-98	40-92	36-98	40-98	48-92	39-95	54-98	40-98	36-98	40-97	48-98	39-97
p-value	-	<0.001*	0.54	0.03*	0.18	0.004*	-	0.003*	0.28	0.01*	0.002*	<0.001*	-	0.002*	0.03*	<0.001*	0.003*	<0.001*

Table 2 reports the mean, standard deviation and range of the correlation coefficients for tumor, necrosis and edema of the HGG patients for all considered datasets. Correlation coefficients are above 0.90 in nearly all cases, indicating that the tissue source vector obtained with hNMF is highly representative for the corresponding tissue region. Higher correlation coefficients are found for some reduced MRI datasets compared to full MP-MRI, and statistical significance of higher correlation coefficients for full MP-MRI could not be shown in most cases. Differences in correlation coefficients are relatively small among the MRI datasets: compared to full MP-MRI, variations ranged from a decrease of 0.06 to an increase of 0.05.

Table 3 shows the Dice-scores for the complete tumor region of the LGG patients for all considered datasets. As necrosis does not occur in LGGs and edema was found within the MRSI ROI in only 1 patient, Dice-scores are only reported for the complete tumor region. The mean Dice-score is 85% for the full MP-MRI dataset and is lower for all reduced MRI datasets. Statistical significance could only be shown compared to no-cMRI, for which the mean Dice-score was 73%. For all other reduced datasets, only a slight decrease in mean Dice-score was found, ranging from 1% to 4%.

Table2: *Mean, standard deviation and range of the correlation coefficients for the HGG patients. Results are reported for tumor, necrosis and edema using the full MP-MRI dataset (light grey), MP-MRI without cMRI, PWI, MRSI and DKI and for cMRI data only. P-values report statistical significance of higher correlation coefficients for the full MP-MRI dataset (* indicates statistical significance for p<0.05).*

	Correlation coefficient tumor						**Correlation coefficient necrosis**						**Correlation coefficient edema**					
	All	**no-cMRI**	**no-PWI**	**no-MRSI**	**no-DKI**	**cMRI only**	**All**	**no-cMRI**	**no-PWI**	**no-MRSI**	**no-DKI**	**cMRI only**	**All**	**no-cMRI**	**no-PWI**	**no-MRSI**	**no-DKI**	**cMRI only**
Mean	**0.91**	**0.92**	**0.89**	**0.85**	**0.96**	**0.87**	**0.97**	**0.92**	**0.97**	**0.95**	**0.95**	**0.94**	**0.96**	**0.93**	**0.94**	**0.93**	**0.97**	**0.93**
Standard deviation	0.09	0.07	0.13	0.16	0.02	0.16	0.03	0.13	0.03	0.06	0.05	0.09	0.04	0.06	0.07	0.07	0.04	0.11
Range [Min-Max]	0.71-0.99	0.76-1	0.63-1	0.54-1	0.93-1	0.59-1	0.90-1	0.58-0.99	0.90-0.99	0.81-1	0.86-0.99	0.70-1	0.90-1	0.84-0.99	0.80-1	0.77-1	0.89-1	0.76-0.99
p-value	-	0.52	0.30	0.12	0.98	0.19	-	0.02*	0.26	0.33	0.04*	0.21	-	0.17	0.19	0.11	0.95	0.56

Table3: *Mean, standard deviation and range of the Dice-scores for the LGG patients. Results are reported for the complete tumor region using the full MP-MRI dataset (light grey), MP-MRI without cMRI, PWI, MRSI and DKI and for cMRI data only. P-values report statistical significance of higher Dice-scores for the full MP-MRI dataset (* indicates statistical significance for p<0.05).*

	Dice-score complete tumor [%]					
	All	**no-cMRI**	**no-PWI**	**no-MRSI**	**no-DKI**	**cMRI only**
Mean	**85**	**73**	**81**	**84**	**84**	**81**
Standard deviation	14	20	15	17	16	18
Range [Min-Max]	50-96	42-95	52-96	41-96	46-96	38-96
p-value	-	0.003*	0.10	0.85	0.32	0.07

Table 4 reports the mean, standard deviation and range of the correlation coefficients for the tumor region of the LGG patients for all considered datasets. The mean correlation coefficient is not lower than 0.90 for any dataset. For the full MP-MRI dataset, a mean correlation coefficient of 0.95 was found. Higher correlation coefficients are obtained for the reduced MRI datasets, except for no-cMRI. The lower correlation coefficient for no-cMRI is probably related to the lower Dice-score, indicating a higher mismatch between the hNMF tumor source and the actual tumor region. The difference in the correlation coefficients was not found to be statistically significant in any case.

Table4: *Mean, standard deviation and range of the correlation coefficients for the LGG patients. Results are reported for tumor using the full MP-MRI dataset (light grey), MP-MRI without cMRI, PWI, MRSI and DKI and for cMRI data only. P-values report statistical significance of higher Dice-scores for the full MP-MRI dataset (* indicates statistical significance for p<0.05).*

	Correlation coefficient tumor					
	All	**no-cMRI**	**no-PWI**	**no-MRSI**	**no-DKI**	**cMRI only**
Mean	**0.95**	**0.90**	**0.96**	**0.98**	**0.98**	**0.97**
Standard deviation	0.08	0.15	0.09	0.03	0.02	0.03
Range [Min-Max]	0.75-1	0.57-1	0.72-1	0.93-1	0.94-1	0.89-1
p-value	-	0.08	0.88	1	0.95	0.81

Discussion

Comparison with previous NMF studies

To the authors' knowledge, this is the first study in which hNMF is applied to multi-parametric MRI data for brain tumor characterization. Several studies have applied NMF to brain tumor MRSI data for tissue differentiation (35,36,55). The concept of hierarchical NMF was introduced in a previous study, reporting improved tissue differentiation for hNMF compared to single-level NMF on simulated as well as in vivo MRSI data of GBM patients (55). Single-level NMF was initially also considered in the current study, but statistically significantly better results were found for hNMF when applied to the MP-MRI. Comparison of single-level NMF and hNMF validation results are reported in Appendix C. The advantage of using MP-MRI data compared to only MRSI data is twofold. Firstly, the higher resolution of the added MRI features will allow a more detailed and accurate delineation of the tumor subregions. Previous studies also considered an hNMF-based segmentation for validation purposes. In Li et al.(55), this validation was only done visually, hampering comparison of the results. Ortega-Martorell et al. (36) did quantify the correspondence between the segmentation obtained from hNMF and post-mortem Ki67 immunostaining applied to 7 GBM bearing mice, resulting in a mean accuracy of 83.7% for the tumor region. However, safe thresholds were applied to the proliferation index obtained from immunostaining for labelling the voxels, such that MRSI voxels near the tumor-normal tissue interface were not always considered. Furthermore, differentiation between tumor and necrosis was not considered. Secondly, the low resolution of the MRSI data results in considerable partial volume effects, with many voxels containing tissue mixtures. Especially in the case of small lesions, there might not be any pure voxels containing only necrosis or tumor, which will make source separation more difficult. Additionally, it was pointed out in (55) that the MRSI spectrum of the tumor source can approximately be modelled as a linear combination of the necrotic and the normal tissue source. This complicates the separability of the tissue types. Adding other MRI features to the dataset will further decorrelate the tissue sources, improving their separability.

The H_{ratio3} criterion that was implemented to find the optimal threshold t in hNMF step3 assumes that most voxels will contain mainly one tissue type. However, when only MRSI data are considered, it is not evident that the same criterion can be applied successfully, given the low spatial resolution of the MRSI data. By applying the optimal threshold t to both the H_{ratio1} and H_{ratio2} map, voxels that contain considerable contributions of both sources after step1 are

not considered for determining the tissue-specific patterns in hNMF step2. Since in step2, each voxel is fully modelled by either the tissue types represented by source1^{step1} or the tissue types represented by source2^{step1}, these mixed voxels will act as a confounding factor for determining the tissue sources. The optimal threshold value *t* varied considerably among patients and there was no clear trend. Lower H_{ratio3} values were usually found at the highest *t*-values, as voxel selection gets so much reduced that one or more tissue types are no longer represented within the voxel selection. In general, the variability of the validation scores as a function of *t* was higher in patients with a higher number of tissue types within the MRSI ROI. In patients with only 2 or 3 tissue types, Dice-scores and correlation coefficients are often rather constant over the *t*-range, such that selection of the optimal threshold gave little improvement.

The rationale behind adding the averaged non-metabolic features with 3×3 and 5×5 averaging windows is twofold. Firstly, some of the original non-metabolic features showed high intra-tissue variability (e.g. rCBV in the viable tumor region), which lead in some cases to a mis-labelling of the 'outlier' voxels. By adding the averaged features, hNMF was better able to cope with this intra-tissue heterogeneity. Secondly, lower Dice-scores were commonly seen in patients due to the low spatial accuracy of the metabolic features, which had more weight in the hNMF results when the averaged features were not included. Statistically significantly higher Dice-scores were obtained for all tissue classes when including the averaged features, in HGGs as well as in LGGs. A comparison of the mean validation scores obtained with and without the averaged features can be found in Appendix D. Previous NMF studies assumed the number of sources/tissue types to be a priori known (36, 55). Automatic detection of the number of sources in NMF is challenging, and none of the proposed methods have reached general applicability (56). A limitation in the current study is that the number of sources had to be set manually for each individual patient. This was done based on visual inspection of the cMRI data by an experienced neuro-radiologist. If the number of sources is set lower than the actual number of tissue types, sources will represent mixtures of tissue types. If the number of sources is set too high, some tissue types will be modelled by more than one source. Future research should therefore focus on reliable automatic assessment of the number of sources.

Reduced MP-MRI datasets and cMRI only

The hNMF procedure was also applied to reduced MP-MRI datasets, leaving out one MRI modality at a time. Compared to the full MP-MRI dataset, mean Dice-scores were lower and the standard deviation was higher for all reduced MP-MRI datasets and for each segmentation task. For the HGG patients, the decrease in mean Dice-score varied between 2% and 8% in all but one case, showing that hNMF still performs well when less MRI modalities are available. A larger decrease in mean Dice-score of 13% was only found for tumor for the no-cMRI dataset. This result shows the importance of T1+C to differentiate tumor from necrosis. For the no-PWI case, Dice-scores were only significantly higher for the complete tumor region. One might expect rCBV to aid in differentiating tumor, due to an increased (micro)vascularity in the HGG viable tumor region. But compared to other MRI features, rCBV shows a large heterogeneity within the viable tumor tissue, with some areas not being well perfused at all (14). In some patients, such low-perfused tumor areas were not delineated as tumor when including PWI, leading to lower Dice-scores for tumor and the tumor core. However, in several other patients rCBV improved tumor delineation, in particular in small HGG lesions which were not easily detected by hNMF. Improved tissue differentiation within brain tumors by adding MRSI to cMRI has been reported before (57) and was also shown to be statistically significant for each class in our study. Despite its low spatial resolution, several metabolites are among the most specific features to detect tumor and necrosis: elevated levels of Lip, Lac and Cho are only expected to be found within the tumor core. In several HGG patients, voxels outside the

pathologic region were wrongfully labelled as tumor or necrosis when omitting MRSI. In addition, small areas of non-enhancing tumor were sometimes not denoted as tumor by hNMF without MRSI. Statistical significance for adding DKI to the full MP-MRI dataset was shown for the tumor core and complete tumor region, but not for viable tumor. As was reported in (25) for MD, inclusion of the DKI parameters improved edema segmentation in several patients. It also resulted in better differentiation of necrosis from edema in some cases. When considering only cMRI data, statistical significance of the higher Dice-scores for full MP-MRI has been shown for each tissue class. Compared to the reduced MP-MRI datasets, a larger decrease in mean Dice-scores was found: 9% for tumor, 14% for the tumor core and 15% for the complete tumor.

For the LGG patients, although the mean Dice-score of the complete tumor region was highest for the full MP-MRI dataset, statistical significance was only shown against no-cMRI, with a decrease in mean Dice-score by 12%. As LGGs represent an earlier stage of the disease, hallmarks such as angiogenesis, hypoxia, necrosis and increased cell proliferation are uncommon. The tumor tissue is mostly differentiable on cMRI and DWI, but with low specificity. Additionally, for no-cMRI the tumor tissue was not properly separated from CSF in some LGG patients, as these tissue types are mostly differentiable based on FLAIR. Since statistical significance could not be shown for the other reduced MRI datasets, it seems that additional MRI modalities do not improve tumor differentiation in most LGG cases.

For both the HGG and the LGG patients, the mean correlation coefficient showed a less distinct decrease in most cases and even a slight increase in some cases compared to full MP-MRI. It must be noted that a higher correlation coefficient does not warrant better tissue differentiation: a significant amount of voxels will not contain purely one tissue type, such that the average feature vector per tissue region is expected to contain some contamination from other tissue types. Since the correlation coefficients are above 0.90 in most cases for the HGG as well as for the LGG patients, the pathologic hNMF sources are representative for the corresponding tissue region and can be considered as patient- and tissue-specific patterns.

Tumor segmentation

Tumor segmentation is a challenging task in the image analysis of brain tumors. Manual delineation is still the gold standard in clinical practice. Nevertheless, it is a time-consuming and user-dependent process, prone to errors and with questionable reproducibility (58). To overcome these limitations, many sophisticated algorithms have been developed for automated segmentation. However, few have achieved the speed, accuracy, and limited user interaction required for routine clinical use. One means of validation was to convert the hNMF results into an absolute voxel-by-voxel segmentation, by applying k-means clustering to the obtained abundance maps. Comparing the hNMF-based segmentation to the manual segmentation by an experienced radiologist, mean Dice-scores for the complete tumor region of 83% and 85% were found for the HGG and the LGG patients, respectively. For the HGGs, mean Dice-scores of 78% and 85% were found for the viable tumor region and for the tumor core, respectively. These Dice-scores are higher than the mean Dice-scores of the best performing methods in (54) reporting on the BRATS challenge 2012-2013 results. It must be noted that these methods are all supervised classification methods which only rely on cMRI data. Nevertheless, it shows that our results are competitive with the state-of-the-art segmentation techniques, even when only cMRI data are considered. We have thus shown that the hNMF method presented in this study can be applied as a valid unsupervised segmentation technique. Another difference with the BRATS challenge is that we did not consider a full 3D imaging dataset, but only a 2D region corresponding to the MRSI ROI, as this is the only region where a full set of MP-MRI features

was available. This is an important limitation of including MRSI, as tissue characterization of the entire tumor volume is mandatory for treatment planning and response monitoring. Although 3D MRSI is available, it is often not possible to cover the entire tumor volume, as the MRSI spatial grid has to be positioned entirely within the brain to avoid artefacts like lipid contamination from the skull. Recently, an echo-planar MRSI sequence has been presented that does allow full coverage of the whole brain (59). Full tumor coverage with MRSI will be possible when such sequences become available for clinical practice.

The relative contribution of each tissue type within each voxel is presented by means of the abundance maps. These maps allow direct visual interpretation of the hNMF results, combining the information of all MRI parameters into one map per tissue type. The relative contributions of different tissue types within the tumor region provide us with more insight in the spatial heterogeneity of the tumor. To further synthesize visual assessment, the abundance maps can be combined into a single nosologic image, in which each tissue class is represented by one colour and colour mixtures are used to quantify the relative contribution of each tissue type in each voxel (60,61).

Unsupervised vs supervised classification

Given the wide range of tumor characteristics that is reported for HGGs and the large heterogeneity that is often seen within the same lesion, unsupervised methods have the advantage of not making any prior assumptions about the expected values of the individual features. This has allowed us to apply hNMF on a patient-by-patient basis, resulting in patient-specific tissue patterns. Several studies have applied supervised classification methods to characterize brain tumor substructures. Di Costanzo et al. applied linear discriminant analysis to MP-MRI data to perform ROI based classification of solid tumor, edema, edema/tumor and infiltrated peri-tumoral tissue on low- and high-grade gliomas (32). Classification accuracy of 67% was found for solid tumor ROIs. Another study used support vector machines on a combination of cMRI and DTI to distinguish enhancing tumor, non-enhancing tumor and edema in high-grade brain tumors (31). Voxel-wise classification rates of 89% and 34% were found for enhancing and non-enhancing tumor, respectively. As was pointed out in the latter study, tumor regions might contain varying degrees of neoplasm combined with healthy tissue or edema. Identifying tissue-specific patterns across patients is hampered due to the co-existence of different tissue types, especially when mixed tissue classes are considered. This aspect of tissue complexity is not taken into consideration by most other classification methods. One limitation of unsupervised methods such as (h)NMF, is that the sources are not automatically labelled. This was done based on visual interpretation of the sources and their abundance maps.

Voxel-wise vs ROI analysis

Previous advanced MRI studies have often considered single statistical values for a lesion, or for a few ROIs within the lesion. Given the heterogeneous nature of HGGs, a simple statistical metric such as the mean value is inadequate in characterizing the whole tumor. Numerous studies have proposed minimum or maximum values of PWI, DWI or MRSI parameters to assess tumor malignancy (9,30) or to detect the most malignant part of the lesion for biopsy targeting (18,62). Such methods, although they have shown statistical significance in most cases, lack robustness against outlier values and have limited interpretability. A more detailed intra-tumoral tissue characterization will allow us to move towards more personalized and dedicated treatment planning.

Acknowledgements
This work has been funded by the following projects: Flemish Government FWO project G.0869.12N (Tumor imaging); IWT IM 135005; Belgian Federal Science Policy Office: IUAP P7/19/ (DYSCO, `Dynamical systems, control and optimization', 2012-2017); Henri Benedictus Fellowship of the Belgian American Educational Foundation; Interuniversity Attraction Poles Program (P7/11) initiated by the Belgian Science Policy Office. VIDI Grant 639.072.411 from the Netherlands Organisation for Scientific Research (NWO). EU: European Research Council under the European Union's Seventh Framework Programme (FP7/2007-2013), ERC Advanced Grant: BIOTENSORS (n°339804) and the EU MC ITN TRANSACT 2012 (n°316679).

References

1. Grant R. Overview: Brain tumour diagnosis and management/Royal College of Physicians guidelines. J. Neurol. Neurosurg. Psychiatry 2004;75 Suppl 2:ii18–23.

2. Louis DN, Ohgaki H, Wiestler OD, Cavenee WK, Burger PC, Jouvet A, Scheithauer BW, Kleihues P. The 2007 WHO classification of tumours of the central nervous system. Acta Neuropathol. (Berl.) 2007;114:97–109.

3. Paulus W, Peiffer J. Intratumoral histologic heterogeneity of gliomas. A quantitative study. Cancer 1989;64:442–7.

4. Jacobs AH, Kracht LW, Gossmann A, Rüger MA, Thomas AV, Thiel A, Herholz K. Imaging in neurooncology. NeuroRx J. Am. Soc. Exp. Neurother. 2005;2:333–47.

5. Jackson RJ, Fuller GN, Abi-Said D, Lang FF, Gokaslan ZL, Shi WM, Wildrick DM, Sawaya R. Limitations of stereotactic biopsy in the initial management of gliomas. Neuro-Oncol. 2001;3:193–200.

6. Earnest F, Kelly PJ, Scheithauer BW, Kall BA, Cascino TL, Ehman RL, Forbes GS, Axley PL. Cerebral astrocytomas: histopathologic correlation of MR and CT contrast enhancement with stereotactic biopsy. Radiology 1988;166:823–7.

7. Van Cauter S, De Keyzer F, Sima DM, Croitor Sava AR, D'Arco F, Veraart J, Peeters R, Leemans A, Van Gool S, Wilms G, Demaerel P, Van Huffel S, Sunaert S, Himmelreich U. Integrating diffusion kurtosis imaging, dynamic susceptibility-weighted contrast-enhanced MRI, and short echo time chemical shift imaging for grading gliomas. Neuro-Oncol.

8. Sugahara T, Korogi Y, Kochi M, Ikushima I, Hirai T, Okuda T, Shigematsu Y, Liang L, Ge Y, Ushio Y, Takahashi M. Correlation of MR imaging-determined cerebral blood volume maps with histologic and angiographic determination of vascularity of gliomas. AJR Am. J. Roentgenol. 1998;171:1479–86.

9. Cha S, Knopp EA, Johnson G, Wetzel SG, Litt AW, Zagzag D. Intracranial mass lesions: dynamic contrast-enhanced susceptibility-weighted echo-planar perfusion MR imaging. Radiology 2002;223:11–29.

10. Bulakbasi N, Kocaoglu M, Farzaliyev A, Tayfun C, Ucoz T, Somuncu I. Assessment of diagnostic accuracy of perfusion MR imaging in primary and metastatic solitary malignant brain tumors. AJNR Am. J. Neuroradiol. 2005;26:2187–99.

11. Young GS. Advanced MRI of adult brain tumors. Neurol. Clin. 2007;25:947–73, viii.

12. Provenzale JM, Wang GR, Brenner T, et al. Comparison of permeability in high-grade and low-grade brain tumors using dynamic susceptibility contrast MR imaging. AJR Am J Roentgenol 2002; 178:711–16

13. Law M, Cha S, Knopp EA, Johnson G, Arnett J, Litt AW. High-grade gliomas and solitary metastases: differentiation by using perfusion and proton spectroscopic MR imaging. Radiology 2002;222:715–21.

14. Lupo JM, Cha S, Chang SM, Nelson SJ. Dynamic susceptibility-weighted perfusion imaging of high-grade gliomas: characterization of spatial heterogeneity. AJNR Am. J. Neuroradiol. 26:1446–54.

15. Maia ACM, Malheiros SMF, da Rocha AJ, Stavale JN, Guimaraes IF, Borges LRR, Santos AJ, da Silva CJ, de Melo JGSP, Lanzoni OP, Gabbai AA, Ferraz FAP. Stereotactic biopsy guidance in adults with supratentorial nonenhancing gliomas: role of perfusion-weighted magnetic resonance imaging. J. Neurosurg. 2004;101:970–6.

16. Law M, Yang S, Wang H, Babb JS, Johnson G, Cha S, Knopp EA, Zagzag D. Glioma grading: sensitivity, specificity, and predictive values of perfusion MR imaging and proton MR spectroscopic imaging compared with conventional MR imaging. AJNR Am. J. Neuroradiol. 24:1989–98.

17. Kuesel AC, Sutherland GR, Halliday W, Smith IC. 1H MRS of high grade astrocytomas: mobile lipid accumulation in necrotic tissue. NMR Biomed. 1994;7:149–55.

18. Wagner M, Nafe R, Jurcoane A, Pilatus U, Franz K, Rieger J, Steinbach JP, Hattingen E. Heterogeneity in malignant gliomas: a magnetic resonance analysis of spatial distribution of metabolite changes and regional blood volume. J. Neurooncol. 2011;103:663–72.

19. Hall WA, Martin A, Liu H, Truwit CL. Improving diagnostic yield in brain biopsy: coupling spectroscopic targeting with real-time needle placement. J. Magn. Reson. Imaging JMRI 2001;13:12–5.

20. Ricci R, Bacci A, Tugnoli V, Battaglia S, Maffei M, Agati R, Leonardi M. Metabolic findings on 3T 1H-MR spectroscopy in peritumoral brain edema. AJNR Am. J. Neuroradiol. 2007;28:1287–91.

21. Le Bihan D. Apparent diffusion coefficient and beyond: what diffusion MR imaging can tell us about tissue structure. Radiology 2013;268:318–22.

22. Bulakbasi N, Guvenc I, Onguru O, Erdogan E, Tayfun C, Ucoz T. The added value of the apparent diffusion coefficient calculation to magnetic resonance imaging in the differentiation and grading of malignant brain tumors. J. Comput. Assist. Tomogr. 28:735–46.

23. Kitis O, Altay H, Calli C, Yunten N, Akalin T, Yurtseven T. Minimum apparent diffusion coefficients in the evaluation of brain tumors. Eur. J. Radiol. 2005;55:393–400.

24. Basser PJ, Mattiello J, LeBihan D. MR diffusion tensor spectroscopy and imaging. Biophys. J. 1994;66:259–67.

25.Sinha S, Bastin ME, Whittle IR, Wardlaw JM. Diffusion tensor MR imaging of high-grade cerebral gliomas. AJNR Am J Neuroradiol. 2002;23(4);520-7.

26. Poot DHJ, den Dekker AJ, Achten E, Verhoye M, Sijbers J. Optimal experimental design for diffusion kurtosis imaging. IEEE Trans. Med. Imaging 2010;29:819–29.

27. Veraart J, Poot DHJ, Van Hecke W, Blockx I, Van der Linden A, Verhoye M, Sijbers J. More accurate estimation of diffusion tensor parameters using diffusion Kurtosis imaging. Magn. Reson. Med. Off. J. Soc. Magn. Reson. Med. Soc. Magn. Reson. Med. 2011;65:138–145.

28. Van Cauter S, Veraart J, Sijbers J, Peeters RR, Himmelreich U, De Keyzer F, Van Gool SW, Van Calenbergh F, De Vleeschouwer S, Van Hecke W, Sunaert S. Gliomas: diffusion kurtosis MR imaging in grading. Radiology 2012;263:492–501.

29. Raab P, Hattingen E, Franz K, Zanella FE, Lanfermann H. Cerebral gliomas: diffusional kurtosis imaging analysis of microstructural differences. Radiology 2010;254:876–81.

30. Zonari P, Baraldi P, Crisi G. Multimodal MRI in the characterization of glial neoplasms: the combined role of single-voxel MR spectroscopy, diffusion imaging and echo-planar perfusion imaging. Neuroradiology 2007;49:795–803.

31. Verma R, Zacharaki EI, Ou Y, Cai H, Chawla S, Lee S-K, Melhem ER, Wolf R, Davatzikos C. Multiparametric tissue characterization of brain neoplasms and their recurrence using pattern classification of MR images. Acad. Radiol. 2008;15:966–77.

32. Di Costanzo A, Scarabino T, Trojsi F, Giannatempo GM, Popolizzio T, Catapano D, Bonavita S, Maggialetti N, Tosetti M, Salvolini U, D'Angelo VA, Tedeschi G. Multiparametric 3T MR approach to the assessment of cerebral gliomas: tumor extent and malignancy. Neuroradiology 2006;48:622–31.

33. Louis DN, Holland EC, Cairncross JG. Glioma Classification. Am. J. Pathol. 2001;159:779–786.

34. Muti M, Aprile I, Principi M, Italiani M, Guiducci A, Giulianelli G, Ottaviano P. Study on the variations of the apparent diffusion coefficient in areas of solid tumor in high grade gliomas. Magn. Reson. Imaging 2002;20:635–41.

35. Sajda P, Du S, Brown TR, Stoyanova R, Shungu DC, Mao X, Parra LC. Nonnegative matrix factorization for rapid recovery of constituent spectra in magnetic resonance chemical shift imaging of the brain. IEEE Trans. Med. Imaging 2004;23:1453–65.

36. Ortega-Martorell S, Lisboa PJG, Vellido A, Simões RV, Pumarola M, Julià-Sapé M, Arús C. Convex non-negative matrix factorization for brain tumor delimitation from MRSI data. PloS One 2012;7:e47824.

37. Dynamic Susceptibility Contrast MR ANalysis (DSCoMAN). Available at: https://dblab.duhs.duke.edu/modules/dscoman/index.php?id=1

38. Schneider CA, Rasband WS, Eliceiri KW. NIH Image to ImageJ: 25 years of image analysis. Nat. Methods 2012;9:671–675.

39. Boxerman JL, Schmainda KM, Weisskoff RM. Relative cerebral blood volume maps corrected for contrast agent extravasation significantly correlate with glioma tumor grade, whereas uncorrected maps do not. AJNR Am. J. Neuroradiol. 2006;27:859–67.

40. Van Cauter S, Sima DM, Luts J, ter Beek L, Ribbens A, Peeters RR, Osorio Garcia MI, Li Y, Sunaert S, Van Gool S, Van Huffel S, Himmelreich U. Reproducibility of rapid short echo time CSI at 3 tesla for clinical applications. J. Magn. Reson. Imaging JMRI 2013;37:445–56.

41. Ogg RJ, Kingsley PB, Taylor JS. WET, a T1- and B1-insensitive water-suppression method for in vivo localized 1H NMR spectroscopy. J. Magn. Reson. B 1994;104:1–10.

42. Poullet J-B, Quantification and classification of magnetic resonance spectroscopic data for brain tumor diagnosis. PhD Thesis, Leuven, 2008. Available at: http://homes.esat.kuleuven.be/~biomed/software.php#SpidGUI

43. Croitor Sava AR, Sima DM, Poullet J-B, Wright AJ, Heerschap A, Van Huffel S. Exploiting spatial information to estimate metabolite levels in two-dimensional MRSI of heterogeneous brain lesions. NMR Biomed. 2011;24:824–35.

44. Poullet J-B, Sima DM, Van Huffel S, Van Hecke P. Frequency-selective quantitation of short-echo time 1H magnetic resonance spectra. J. Magn. Reson. San Diego Calif 1997 2007;186:293–304.

45. Andersson J, Xu J, Yacoub E. A comprehensive Gaussian process framework for correcting distortions and movements in diffusion images. In: Proceedings of the 20th Annual Meeting of ISMRM. ; 2012.

46. Veraart J, Sijbers J, Sunaert S, Leemans A, Jeurissen B. Weighted linear least squares estimation of diffusion MRI parameters: strengths, limitations, and pitfalls. NeuroImage 2013;81:335–346.

47. Le Bihan D, Mangin JF, Poupon C, Clark CA, Pappata S, Molko N, Chabriat H. Diffusion tensor imaging: concepts and applications. J. Magn. Reson. Imaging JMRI 2001;13:534–46.

48. Statistical Parametric Mapping (SPM). Available at: http://www.fil.ion.ucl.ac.uk/spm/

49. Maes F, Collignon A, Vandermeulen D, Marchal G, Suetens P. Multimodality image registration by maximization of mutual information. IEEE Trans. Med. Imaging 1997;16:187–98.

50. Leemans A, Jeurissen B, Sijbers J, Jones D. ExploreDTI: a graphical toolbox for processing, analyzing, and visualizing diffusion MR data. In: 17th Annual Meeting of Intl Soc Mag Reson Med. Hawaï, USA; 2009. p. 3537.

51. Lee DD, Seung HS. Learning the parts of objects by non-negative matrix factorization. Nature 1999;401:788–91.

52. Gillis N, Glineur F. Accelerated multiplicative updates and hierarchical ALS algorithms for nonnegative matrix factorization. Neural Comput. 2012;24:1085–105.

53. Li Y, Sima D, Van Cauter S, Himmelreich U, Pi Y, Van Huffel S. Simulation study of tissue type differentiation using non-negative matrix factorization. In: Proceedings of BIOSIGNALS 2012. Algarve, Portugal; 2012. pp. 212–217.

54. Menze B, Jakab A, Bauer S, Kalpathy-Cramer J, Farahani K, et al. The Multimodal Brain Tumor Image Segmentation Benchmark (BRATS). IEEE Transactions on Medical Imaging, Institute of Electrical and Electronics Engineers (IEEE), 2014, pp.33. hal-00935640v2

55. Li Y, Sima DM, Cauter SV, Croitor Sava AR, Himmelreich U, Pi Y, Van Huffel S. Hierarchical non-negative matrix factorization (hNMF): a tissue pattern differentiation method for glioblastoma multiforme diagnosis using MRSI. NMR Biomed. 2013;26:307–19.

56. Wang Y, Zhang Y. Nonnegative Matrix Factorization: A Comprehensive Review. IEEE Trans Knowl Data En. 2013;25:1336-53.

57. Luts J, Laudadio T, Idema AJ, Simonetti AW, Heerschap A, Vandermeulen D, Suykens JAK, Van Huffel S. Nosologic imaging of the brain: segmentation and classification using MRI and MRSI. NMR Biomed 2009;22(4):374-390.

58. Mazzara GP, Velthuizen RP, Pearlman JL, Greenberg HM, Wagner H. Brain tumor target volume determination for radiation treatment planning through automated MRI segmentation. Int. J. Radiat. Oncol. Biol. Phys. 2004;59:300–12.

59. Maudsley A, Domenig C, Govind V, Darkazanli A, Studholme C, Arheart K, Bloomer C. Mapping of brain metabolite distributions by volumetric proton MR spectroscopic imaging (MRSI). Magn Reson Med. 2009;61(3):548-59.

60. Li Y, Sima DM, Van Cauter S, Himmelreich U, Croitor Sava AR, Pi Y, Liu Y, Van Huffel S. Unsupervised nosologic imaging for glioma diagnosis. IEEE Trans. Biomed. Eng. 2013;60:1760–3.

61. Laudadio T, Martínez-Bisbal MC, Celda B, Van Huffel S. Fast nosological imaging using canonical correlation analysis of brain data obtained by two-dimensional turbo spectroscopic imaging. NMR Biomed. 2008;21:311–21.

62. Weber M-A, Henze M, Tüttenberg J, Stieljes B, Meissner M, Zimmer F, Burkholder I, Kroll A, Combs SE, Vogt-Schaden M, Giesel F, Zoubaa S, Haberkorn U, Kauczor HU, Essig M. Biopsy targeting gliomas: do functional imaging techniques identify similar target areas? Invest. Radiol. 2010;45:755–68.